Computational Tool

GROmaρs: A GROMACS-Based Toolset to Analyze Density Maps Derived from Molecular Dynamics Simulations

Rodolfo Briones,[1] Christian Blau,[2] Carsten Kutzner,[3] Bert L. de Groot,[3] and Camilo Aponte-Santamaría[4,5,*]

[1]Computational Neurophysiology Group, Institute of Complex Systems 4, Forschungszentrum Jülich, Jülich, Germany; [2]Department of Biochemistry and Biophysics, Science for Life Laboratory, Stockholms Universitet, Stockholm, Sweden; [3]Department of Theoretical and Computational Biophysics, Max Planck Institute for Biophysical Chemistry, Göttingen, Germany; [4]Max Planck Tandem Group in Computational Biophysics, University of Los Andes, Bogotá, Colombia; and [5]Interdisciplinary Center for Scientific Computing, Heidelberg University, Heidelberg, Germany

ABSTRACT   We introduce a computational toolset, named GROmaρs, to obtain and compare time-averaged density maps from molecular dynamics simulations. GROmaρs efficiently computes density maps by fast multi-Gaussian spreading of atomic densities onto a three-dimensional grid. It complements existing map-based tools by enabling spatial inspection of atomic average localization during the simulations. Most importantly, it allows the comparison between computed and reference maps (e.g., experimental) through calculation of difference maps and local and time-resolved global correlation. These comparison operations proved useful to quantitatively contrast perturbed and control simulation data sets and to examine how much biomolecular systems resemble both synthetic and experimental density maps. This was especially advantageous for multimolecule systems in which standard comparisons like RMSDs are difficult to compute. In addition, GROmaρs incorporates absolute and relative spatial free-energy estimates to provide an energetic picture of atomistic localization. This is an open-source GROMACS-based toolset, thus allowing for static or dynamic selection of atoms or even coarse-grained beads for the density calculation. Furthermore, masking of regions was implemented to speed up calculations and to facilitate the comparison with experimental maps. Beyond map comparison, GROmaρs provides a straightforward method to detect solvent cavities and average charge distribution in biomolecular systems. We employed all these functionalities to inspect the localization of lipid and water molecules in aquaporin systems, the binding of cholesterol to the G protein coupled chemokine receptor type 4, and the identification of permeation pathways through the dermicidin antimicrobial channel. Based on these examples, we anticipate a high applicability of GROmaρs for the analysis of molecular dynamics simulations and their comparison with experimentally determined densities.

INTRODUCTION

Molecular dynamics (MD) is a well-established method for the study of biomolecular systems. By monitoring the time evolution of these systems at atomic (or quasiatomic) level or resolution, MD provides key structural, energetic, and (thermo)dynamic information. This information has been instrumental in uncovering the molecular mechanisms of a growing number of bio-macromolecular systems at an unprecedentedly broad spatiotemporal scale range (1).

An inherent challenge of MD is the a posteriori analysis of the simulations. MD users are typically confronted with complex trajectories of hundreds of thousands or even millions of atoms generated by the simulations. To extract relevant information from this large amount of data, it is usually important to focus the analyses to particular regions of interest. Molecular visualization programs such as VMD (2), PyMOL (3), or CHIMERA (4) have greatly contributed to this task by allowing a visual inspection of MD simulations. Moreover, MD packages such as GROMACS (5), NAMD (6) via VMD, AMBER (7), or CHARMM (8) contain plenty of subpackages to quantitatively analyze MD trajectories. In addition, there are a handful of external tools and scripts (9–12) to compute observables from MD simulations.

Because of the dynamic nature of a trajectory, atoms and molecules might exchange positions. If the region of interest is localized, such as a binding pocket or a protein surface, multiple molecules such as solvent or lipids may visit

such locations during the course of a simulation. Therefore, density maps, which average over the identity of individual molecules, are a natural choice for analyses in such cases. In fact, different tools have been developed to include this functionality (GridMAT (13), g_lomepro (14), volmap in VMD (2,15), or PackMem (16), among others).

Likewise, atomistic density maps are ubiquitous to structural biology. Obtained by experimental techniques such as x-ray crystallography, cryo-electron microscopy (cryo-EM), or cryo-electron crystallograpy (cryo-EC), density maps enable the determination of the structure of bio-macromolecules and their assemblies. In practical terms, density maps have the advantage to work at a grid level, therefore allowing straightforward analysis operations such as difference, correlation between maps, or region masking. In fact, structural biology suites (e.g., PHENIX (17) or CCP4 (18)) and visualization packages (like those mentioned above (2–4)) routinely handle and operate with density maps.

The use of density maps in MD simulations, not only for analysis but also for structure refinement, is becoming increasingly popular with experimentally biased methodologies in which structural models are fitted, for instance, into x-ray or cryo-EM density maps (19,20). Moreover, packages such as CHIMERA (4) or VMD (2) offer modules to compute occupancy maps from a structure ensemble, e.g., representing different snapshots of an MD trajectory. Apart from the occupancy, the possibility of using density maps to compare sets of MD simulations has been less explored by the current available tools.

Here, we exploit this possibility by introducing GROmaρs, an open-source GROMACS-based toolset, to efficiently compute and compare time-averaged density maps derived from MD simulations. GROmaρs produces density maps that allow us to spatially inspect the average location of atoms of interest during a simulation. Thus, it constitutes an alternative to the current map-based tools designed for this purpose. Most importantly, GROmaρs expands these tools by enabling quantitative comparison of the computed map with a reference map derived, for instance, from experiments or control simulations. In this work, we describe the methods behind GROmaρs and illustrate its comparison capabilities by revealing important details of the localization of lipids and water molecules around and inside two aquaporin membrane proteins, the binding of cholesterol at the surface of CXCR4, and the solute permeation through the dermicidin antimicrobial channel.

METHODS

Density maps derived from MD simulations

Let us consider a group of N atoms whose time-dependent coordinates are $\mathbf{r}_i(t)$, with $i = 1...N$. We define a three-dimensional lattice, enclosing the N atoms, of dimensions L_x, L_y, and L_z along the x, y, and z axes, respectively (Fig. 1 A). The lattice position is defined by the vector $\mathbf{L}_{min}$
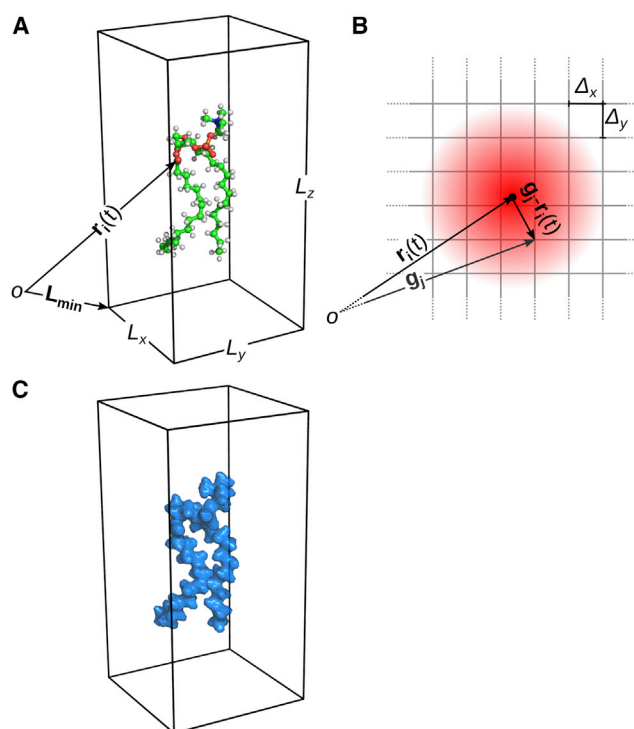

FIGURE 1 Density maps from atomic positions. (A) A group of N atoms is considered (here, a lipid molecule). The position of the i-th atom is $\mathbf{r}_i(t)$. A lattice enclosing the N atoms of dimensions (L_x, L_y, L_z) and origin defined by the vector $\mathbf{L}_{min}$ is considered. (B) Atomic Gaussian spreading on the lattice is sketched for one atom in red. Spreading is shown in two dimensions for clarity. The density contribution of the i-th atom at the lattice position $\mathbf{g}_j$ depends on the separation $|\mathbf{g}_j - \mathbf{r}_i(t)|$. Lattice resolution is indicated at the top right corner. (C) The resulting density map for the lipid molecule is obtained by summing up all atomic contributions onto all lattice points (contoured at 1σ). For MD trajectories, the density map is time averaged over an ensemble of positions sampled by the group of atoms. To see this figure in color, go online.

(Fig. 1 A). The lattice is divided into N_x, N_y, and N_z bins, thus yielding a resolution of $\Delta_x = L_x/N_x$, $\Delta_y = L_y/N_y$, and $\Delta_z = L_z/N_z$ along the three principal coordinate axes (Fig. 1 B). The coordinates of the j-th lattice point are given by the vector $\mathbf{g}_j$.

We assume that each atom spreads isotropically and model the spatial decay of the atomic density with a linear combination of N_G Gaussians. For a point located at a distance d from the atom, the density reads

$$P(d) = \sum_{g=1}^{N_G} A_g e^{-B_g d^2}. \tag{1}$$

Here, A_g and B_g are coefficients that change depending on the atom type. These coefficients can be obtained from the atomic scattering factors—typically fitted by using $N_G = 2$, 4, or 5 Gaussians—from x-ray crystallography or electron microscopy data. Gaussians are by default truncated after five standard deviations, SDs (neglecting less than 1.5×10^{-5} of the total integrated density). The density at each lattice point is estimated by summing up the P contributions from all atoms to that point (Fig. 1 B):

$$\rho(j, t) = \sum_{i=1}^{N} P\left(\left|\mathbf{g_j} - \mathbf{r_i}(t)\right|\right). \tag{2}$$

To reduce the computational cost of evaluating the Gaussian functions at many grid points, we take advantage of the factorization of the Gaussian function in Eq. 1, as suggested in (21). The average density is computed as the ensemble average, for example, recovered from an MD simulation from S discrete, equally spaced time steps t_n as

$$\overline{\rho(j)} = \frac{1}{S} \sum_{n=1}^{S} \rho(j, t_n). \qquad (3)$$

Accordingly, an estimate of the SD of the density reads

$$\sigma^2(\rho(j)) = \frac{1}{S-1} \sum_{n=1}^{S} \left(\rho(j, t_n) - \overline{\rho(j)} \right)^2. \qquad (4)$$

Therefore, the density map produced by GROmaρs consists of the time average and the SD of the density, computed by using Eqs. 3 and 4, at all grid points j of the lattice.

Comparison with a reference density map

GROmaρs allows the comparison of the computed density map with an external reference map, ρ_{ref}. This reference map may be derived, for instance, from a control simulation or an experimentally determined map from x-ray crystallography, cryo-EM, or cryo-EC. Several arithmetic and statistical operations are enabled to quantitatively compare the maps.

Difference density maps

A difference map is calculated by subtracting the reference from the computed map:

$$\Delta\rho(j) = \overline{\rho(j)} - \rho_{ref}(j). \qquad (5)$$

$\Delta\rho(j)$ allows to detect the changes in the average atomic localization, for instance, of a perturbed simulation in comparison to a control simulation.

Global correlation

A global correlation coefficient (cc) between the computed and the reference map is retrieved as

$$cc = \frac{\sum_j \left[\overline{\rho(j)} - \mu \right] \times [\rho_{ref}(j) - \mu_{ref}]}{\left\{ \sum_j \left[\overline{\rho(j)} - \mu \right]^2 \times \sum_j [\rho_{ref}(j) - \mu_{ref}]^2 \right\}^{\frac{1}{2}}}, \qquad (6)$$

where the summations add up all the j points of the density map. Here, μ and μ_{ref} denote the spatial mean of the density maps $\overline{\rho}$ and ρ_{ref}, respectively. The global correlation is also obtained in a time-resolved fashion by block averaging the density for a moving time window of size Δt. Accordingly, for each time $t \geq \Delta t$, the density map entering into Eq. 6 corresponds to that obtained within the time range $[t - \Delta t, t]$.

Local correlation

The local correlation at different points of the lattice is computed, following a similar implementation as the one from CHIMERA (4). A small cubic lattice of size r_{local} in each dimension is considered. The cubic lattice is centered at a grid position j. Subsequently, the correlation coefficient between the computed map and the reference map is obtained using Eq. 6, but only considering the grid points that are within the cubic lattice. The resulting value is stored at the center grid point j. The process is repeated by sliding the cubic lattice over the space, thus yielding a local correlation map. To avoid a different number of grid points in the calculation, the

grid points at the borders of thickness $r_{local}/2$ of the original lattice are not considered as centers for the cubic lattice. Hence, the correlation map has a reduced number of bins along the three principal axes.

Spatial free energy

Absolute ($G_{abs}(j)$) and relative ($G_{rel}(j)$) spatial free-energy estimates are defined according to the formulas

$$G_{abs}(j) = G_0 - \ln\left(\overline{\rho(j)} \right) \qquad (7)$$

and

$$G_{rel}(j) = G_0 - \ln\left(\frac{\overline{\rho(j)}}{\rho_{ref}(j)} \right). \qquad (8)$$

Here, G_0 is an arbitrarily chosen reference value. These two values permit us to obtain an energetic picture of the atomistic localization, by contrasting different regions within the same map (absolute estimate) or different maps at the same position (relative estimate). Regions of zero density can be masked to avoid singularities in the calculation (see Atom Selection and Region Masking below).

Atom selection and region masking

A density calculation may be restricted to a fixed or a dynamic set of atoms, e.g., protein atoms for the former or ligand atoms located within 5 Å from a protein for the latter. In addition, GROmaρs allows us to mask regions using an external map file with the same geometry and resolution of the computed density map. The mask value at the j-th lattice point is $M(j)$. Accordingly, if $M(j)$ is smaller than a threshold mask cutoff M_{cutoff}, then the calculation of the average density at this point is excluded:

$$\overline{\rho(j)} \text{ is} \begin{cases} \text{masked,} & \text{if } M(j) < M_{cutoff} \\ \text{unmasked,} & \text{otherwise.} \end{cases} \qquad (9)$$

The masking attribute allows to focus the comparison between maps within regions of interest that cannot be specified by atom selections. Accordingly, comparison operations are carried out only for the unmasked points. If no external mask map is provided, then the whole lattice is considered for the comparison.

Simulation and density-calculation details

Gaussian coefficients (A_g and B_g) were derived from electron crystallography structure factors (22). These values were set as the default values of the toolset, although any other arbitrary set can be specified by the user. The toolset features are illustrated through four membrane protein examples (see below), although its applicability is not restricted to these types of proteins. Previous MD trajectories (23–26) and experimental density maps (24,27) were considered. See trajectory preparation and density-calculation details in the Supporting Materials and Methods.

RESULTS AND DISCUSSION

Difference maps: Comparison between perturbed and control simulations

We studied the localization of lipids around aquaporin-0 (AQP0) to illustrate the basic features of GROmaρs. AQP0 is the most abundant protein in the eye lens, where

it acts as an anchor between membrane junctions (28) (Fig. 2 A). AQP0 is an ideal system to systematically assess lipid-protein interactions in biological membranes with both cryo-EC (27,29,30) and MD simulations (23,31,32). As a validation of our implementation, we first reproduced with GROmaρs the density maps we obtained earlier for dimyristoylglycerophosphocholine (DMPC) lipids (23). In fact, we obtained identical maps as before, highlighting that annular lipids display a high level of localization, whereas bulk lipids show smearing of their positions (31) (Fig. 2, B and C). We then computed with GROmaρs a difference map to contrast a perturbed and a control simulation. In the perturbed simulation, AQP0 was maintained as a rigid body, whereas the lipids, water molecules, and ions were fully flexible (Fig. 2 B). In the control simulation, AQP0 was also fully flexible (23) (Fig. 2 C). The difference map revealed regions with increased density (*blue*), which is an indication of stronger localization for the acyl chains in front of the rigid AQP0 (Fig. 2 D). The reduced-density red areas (*red*) corresponded mainly to zones affected by the protein expansion in the unrestrained control simulation, which were not visited in the restrained simulations. By symmetry, the lipid-exposed protein surface could be divided into two adjacent surfaces, S1 and S2 (Fig. 2 A). Increments in the density are more notable on the S2 surface, which was found to be more rigid than S1. Difference maps are routinely computed in crystallography. Here, by applying the same strategy to maps derived from MD simulations, we could visually stress the effect of protein mobility on the localization of annular lipids (31).

Correlation between MD and experimental maps

We next examined for the DMPC-AQP0 system the correlation between the map obtained from MD simulations and the map determined by cryo-EC (Fig. 3). In the simulations, the protein was free to move. To focus on the annular lipids, we masked all the lattice voxels except those overlapping with the solved cryo-EC annular-lipid positions (Fig. 3 A). The global correlation coefficient was 0.40 for S1 and 0.49 for S2. Despite the moderate global correlation, the local correlation map displayed regions of high correlation (Fig. 3 B). In particular, at the crystallographic position
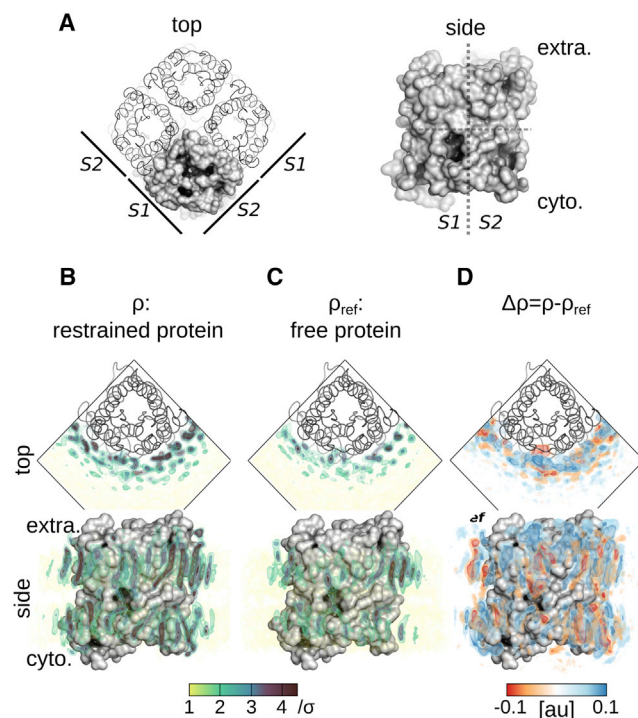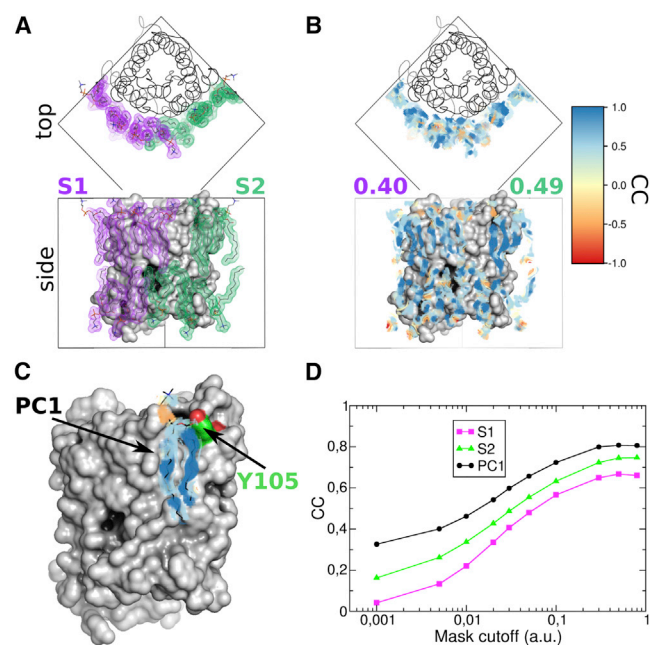

FIGURE 2 Difference map highlights changes between perturbed and control simulations (*A*). Aquaporin-0 (AQP0) is displayed (tetramer: cartoon and one monomer: surface). (*B* and *C*) Normalized density maps for DMPC lipids (*color*) around an AQP0 monomer (*gray*) are shown. The protein was position restrained (*B*: ρ) or free to move (*C*: ρ_{ref}). (*D*) The difference map between the perturbed and the reference map is displayed ($\Delta\rho = \rho - \rho_{ref}$). The density is contoured as isosurfaces at different SD levels (σ) in (*B* and *C*) and at absolute arbitrary units (au) in (*D*). In all panels, top and side views are displayed (extra: extracellular; intra: intracellular, and S1 and S2: surface sides for each monomer). To see this figure in color, go online.

FIGURE 3 Correlation between MD and experimental maps (*A*). Crystallographic annular-lipid positions (*color*) around AQP0 (*black*) were considered for the correlation calculation. The remaining regions were masked. The lipid masks were separated by symmetry into surface S1 (*magenta*) and S2 (*green*). (*B*) Local correlation map around AQP0 is displayed in color according to the color scale at the right. Global correlation values at surfaces S1 and S2 are indicated. (*C*) The local correlation map near the crystallographic lipid PC1 is depicted (same color code as in *B*). (*D*) Global correlation as a function of the mask cutoff, M_{cutoff}, is presented for the indicated regions. The correlation maps presented in (*B*) and (*C*) correspond to $M_{cutoff} = 0.03$ and 0.02, respectively. To see this figure in color, go online.

PC1, the global correlation coefficient was found to be 0.54, and this value locally increased up to values of up to 0.8 (Fig. 3 C). We observed that the global correlation increased when increasing the masked region by augmenting the mask cutoff M_{cutoff} (Fig. 3 D). This suggest that for the regions of high lipid localization (high density), there is a good correspondence between the experimental and the MD maps. In contrast, diffuse experimental lipid positions (low density) cannot be uniquely attributed to the smearing out of the density by the lipid dynamics in the simulations. The correlation analysis presented here thus allowed us to expand our previous studies (23,31) by including a more quantitative comparison of the cryo-EC and the MD data sets.

Time-resolved global correlation

We next examined the localization of water molecules inside the yeast aquaporin channel, Aqy1 (Fig. 4 A). Aqy1 aids yeast to counteract sudden osmotic shocks by regulating membrane water permeation through a gating mechanism involving phosphorylation and potentially membrane-mediated mechanical stress (33). Because the water molecules inside the Aqy1 pore are constantly
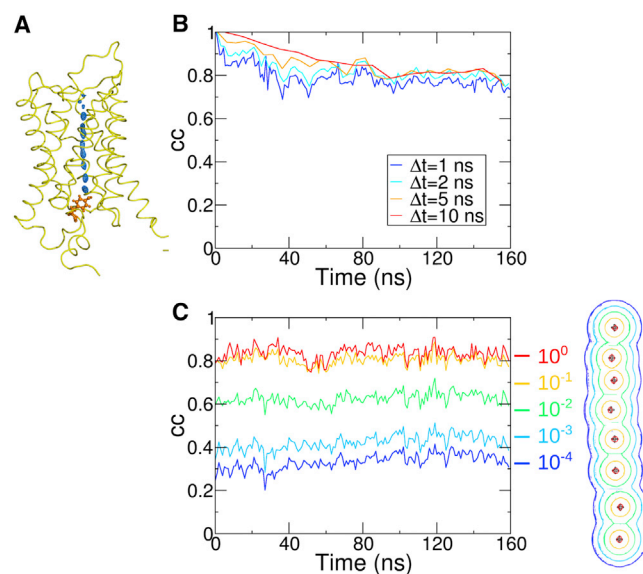

FIGURE 4 Time-resolved global correlation allows to monitor how much multimolecule systems deviate from initial (or reference) states. (A) The x-ray structure of yeast aquaporin (Aqy1) is shown (24) (backbone: *yellow*, tyrosine residue occluding the pore at the cytoplasmic side: *orange*, and electron density associated to the water molecules inside the pore: contoured in *blue* at $\sigma = 1.5$). (B) The density map was computed for the water molecules inside the Aqy1 pore for different time windows Δt. The correlation coefficient (cc) between the computed map and the map calculated for the first time window ([0, Δt]) is presented as a function of the time. (C) The cc of the computed map and the x-ray density map is depicted as a function of the time. The calculation was restricted to the volumes enclosing the crystallographic water molecules depicted at the right side (cystallographic positions: *red* + *symbols*). The color indicates the mask cutoff value M_{cutoff}. To see this figure in color, go online.

exchanging their positions (among themselves and also with water molecules from the bulk media), it is difficult to establish how much they deviate from their original (or other reference) positions with conventional similarity measures such as root-mean-square deviations (RMSDs). To tackle this difficulty, we computed the density map of this set of water molecules within time windows Δt and determined the correlation coefficient with the map computed during the first time window (Fig. 4 B). The correlation stabilized at around a value of 0.8 after ~40 ns of relaxation, thereby indicating that inside the channel, the water positions preserved a high correlation with the initial water localization. Note that increasing Δt increased the relaxation time (by about twofold), but the correlation converged to the same value. We also considered the x-ray density map (24) as a reference for the correlation calculation (Fig. 4 C). We restricted the calculations to a volume that enclosed the crystallographic water molecules by masking the rest of the space (Fig. 4 C, *right*). Because 40 ns of equilibration preceded this simulation (and this part was omitted from this analysis), the correlation coefficient did not start at a value of one but at lower values. Subsequently, the correlation coefficient fluctuated around a converged value that increased by reducing the considered volume enclosing the crystallographic water molecules. The high correlation encountered here for small enclosing volumes is consistent with our previous observation that the average positions of the water molecules inside the channel (related to local minima in the free-energy profile along the pore coordinate) agree well with the x-ray crystallographic positions (24). When extending to larger volumes, energetically unstable regions are also considered, and they may not be captured comparably well in the simulation and in the experiment. In addition, the density of the protein atoms contributed to the x-ray map but not to the MD-computed map. These two may be the reasons for the low correlation for large enclosing volumes. Overall, the time-resolved correlation analysis presented here allowed us to quantitatively monitor how much this multimolecular system deviates from its initial state (Fig. 4 B) and to expand the comparison between simulated and experimental data beyond average positions (Fig. 4 C). This type of analysis is extremely useful to compare non-covalently bonded multimolecular systems, for which conventional similarity measures, like the RMSD, are difficult to obtain.

Spatial free energies: An energetic view of atomic localization

In this example, the energetics associated to the localization of cholesterol molecules around the transmembrane G protein coupled chemokine receptor type 4 (CXCR4) was evaluated. The function of this important receptor has been shown to depend on the cholesterol level in the membrane (25,34). From the study of Pluhackova et al. (25), we took

Briones et al.

a 1-μs coarse-grained (CG) MD trajectory of CXCR4 embedded in a lipid bilayer composed of 1-palmitoyl-2-oleoyl-sn-glycero-3-phosphocholine (POPC) and cholesterol ($\sim$1:10 cholesterol/POPC ratio). We computed spatial free energy maps for cholesterol as defined by Eqs. 7 and 8 (Fig. 5). We considered scaled Gaussian coefficients for the CG beads (see details in the Supporting Materials and Methods). The absolute free energy map revealed regions at the protein surface that were energetically favorable for cholesterol binding (Fig. 5 A). These regions might be considered as sites with moderate binding affinity because these presented a difference of $\sim$−2.0 k_BT with respect to the bulk regions. The relative free energy map displayed the localization of cholesterol weighted by that of POPC lipids (Fig. 5 B). Distant from the protein, the 1:10 cholesterol/POPC ratio resulted in a relative free-energy difference of $\sim$2.3 k_BT. At the cholesterol binding sites on the surface of the protein, the difference shifted toward a higher affinity for cholesterol by at least 1.0 k_BT from the bulk value. In consequence, representation of the density in terms of spatial free energies shows an energetic picture of the cholesterol localization. These results also demonstrate that the chosen Gaussian coefficients properly account for the spreading of CG beads, extending the GROmaρs application range from all-atom to CG systems.

Beyond map comparison: GROmaρs as path and charge distribution finder

In the last example, we explored the potential of GROmaρs to detect pathways and cavities through biomolecules and to determine charge distributions. We considered dermicidin, a human antimicrobial membrane channel, which reduces *Staphylococcus aureus* growth on the epidermal surface (35). This channel is an interesting test system because it ac-
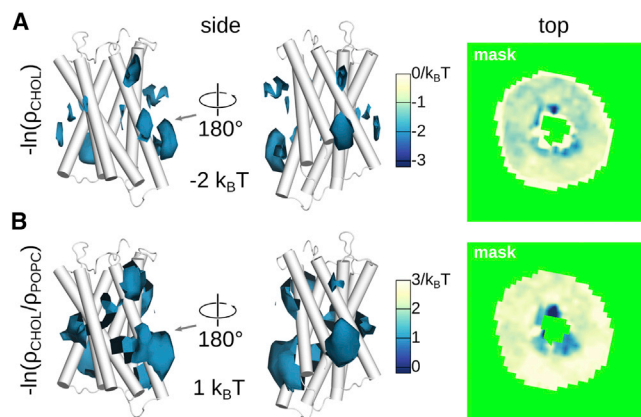
commodates in a tilted position inside the membrane and allows the passage of ions through an unusual side pathway (26) (Fig. 6 A). We took the last 75 ns of a previous 150-ns all-atom simulation of dermicidin embedded in a mixed lipid bilayer, which was fully solvated by explicit water molecules (26). The density map of all the water molecules of the system revealed the tilted channel connecting the two water compartments and, in addition, a small side cavity (Fig. 6 B). In fact, ions use this side path either to exit or to enter the channel (26). Thus, GROmaρs constitutes a straightforward tool to detect pathways through channels and in general cavities through biomolecules, provided that solvent molecules (water molecules in our case) fill these cavities. GROmaρs is thus complementary to the pool of packages created for this purpose (HOLE (36), MOLE (37), and CAVER (38), among others). When the partial charges of the atoms are spread instead of the atomic densities, the resulting map corresponds to the average charge distribution, as presented for dermicidin in Fig. 6 C. Hence, another extension of GROmaρs is to help describe the average charge distribution of biomolecular systems.

CONCLUSIONS

Here, we present GROmaρs, an open-source GROMACS-based toolset for the efficient calculation and comparison
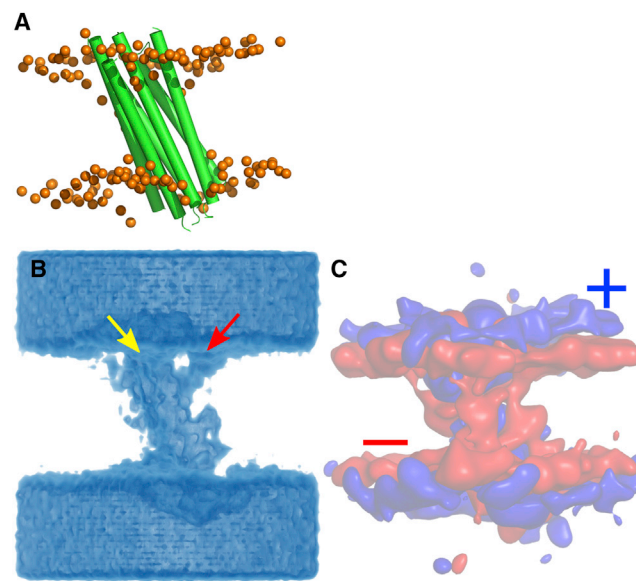
FIGURE 6 GROmaρs applications beyond map comparison include the finding of cavities and charge distributions of biomolecules. (A) The dermicidin antimicrobial channel (*green*) is found in a tilted conformation inside a phospholipid bilayer (phosphorous atoms: *orange*) (26). (B). The density map of the water molecules around and inside the bilayer revealed a main (*yellow arrow*) and an unconventional (*red arrow*) conduction pathway for the passage of solutes. The density is shown in volume representation, contouring it at blue-shade values of 0.6, 1.0, and 1.4 σ. (C) The charge density of dermicidin, lipid molecules, and ions is contoured at two arbitrary (negative and positive) values. To see this figure in color, go online.

FIGURE 5 Spatial free energy for cholesterol (*color*) around CXCR4 (*white cartoon*) is shown. Absolute (A) and relative (B) estimates are presented (*side views*: *left*, and *top view*: *right*). Top view was taken at the height indicated with the gray arrows. Spatial free energy is color coded according to the shown scales. The region shown in green was masked. To see this figure in color, go online.

of density maps from MD simulations. GROma*ρ*s represents an alternative to current map-based methodologies (2,4,13,14,16) to visually inspect the average location of atoms of interest during simulations. Most notably, GROma*ρ*s uses the concepts of density maps used in structural biology, such as difference and correlation maps, to allow the comparison of perturbed and control MD data sets, as well as MD and experimental information. It is a powerful method to tackle multimolecular simulations for which RMSD or related comparison operations are not straightforward. GROma*ρ*s exploits the power of working with densities rather than with atomic positions, and its functionalities revealed important localization details of various biomolecular test systems. Therefore, we consider this tool to be of high applicability for the analysis of biomolecular simulations and their comparison with experimental data.

GROma*ρ*s is available at the site https://mptg-cbp.github.io/gromaps.html.

SUPPORTING MATERIAL

Supporting Materials and Methods, one figure, and one table are available at http://www.biophysj.org/biophysj/supplemental/S0006-3495(18)34448-5.

AUTHOR CONTRIBUTIONS

C.A.-S., R.B., and B.L.d.G. designed research. C.A.-S., C.B., and C.K. implemented the tool. C.A.-S., R.B., and C.K. carried out the tests. All authors discussed and analyzed the data and wrote the manuscript.

ACKNOWLEDGMENTS

SUPPORTING CITATIONS

References (3,5,22–27,39) appear in the Supporting Material.

REFERENCES

1. Dror, R. O., R. M. Dirks, …, D. E. Shaw. 2012. Biomolecular simulation: a computational microscope for molecular biology. *Annu. Rev. Biophys.* 41:429–452.

2. Humphrey, W., A. Dalke, and K. Schulten. 1996. VMD: visual molecular dynamics. *J. Mol. Graph.* 14:33–38, 27–28..

3. 2015. The PyMOL Molecular Graphics System, Version 1.8: Schrödinger, LLC.

4. Pettersen, E. F., T. D. Goddard, …, T. E. Ferrin. 2004. UCSF Chimera—a visualization system for exploratory research and analysis. *J. Comput. Chem.* 25:1605–1612.

5. Abraham, M. J., T. Murtola, …, E. Lindahl. 2015. GROMACS: high performance molecular simulations through multi-level parallelism from laptops to supercomputers. *SoftwareX.* 1–2:19–25.

6. Phillips, J. C., R. Braun, …, K. Schulten. 2005. Scalable molecular dynamics with NAMD. *J. Comput. Chem.* 26:1781–1802.

7. Case, D. A., T. E. Cheatham, III, …, R. J. Woods. 2005. The Amber biomolecular simulation programs. *J. Comput. Chem.* 26:1668–1688.

8. Brooks, B. R., C. L. Brooks, III, …, M. Karplus. 2009. CHARMM: the biomolecular simulation program. *J. Comput. Chem.* 30:1545–1614.

9. McGibbon, R. T., K. A. Beauchamp, …, V. S. Pande. 2015. MDTraj: a modern open library for the analysis of molecular dynamics trajectories. *Biophys. J.* 109:1528–1532.

10. Michaud-Agrawal, N., E. J. Denning, …, O. Beckstein. 2011. MDAnalysis: a toolkit for the analysis of molecular dynamics simulations. *J. Comput. Chem.* 32:2319–2327.

11. Gowers, R. J., M. Linke, …, O. Beckstein. 2016. MDAnalysis: a Python package for the rapid analysis of molecular dynamics simulations. *In* Proceedings of the 15th Python in Science Conference. SciPy, pp. 98–105.

12. Mercadante, D., F. Gräter, and C. Daday. 2018. CONAN: a tool to decode dynamical information from molecular interaction Maps. *Biophys. J.* 114:1267–1273.

13. Allen, W. J., J. A. Lemkul, and D. R. Bevan. 2009. GridMAT-MD: a grid-based membrane analysis tool for use with molecular dynamics. *J. Comput. Chem.* 30:1952–1958.

14. Gapsys, V., B. L. de Groot, and R. Briones. 2013. Computational analysis of local membrane properties. *J. Comput. Aided Mol. Des.* 27:845–858.

15. Cohen, J., A. Arkhipov, …, K. Schulten. 2006. Imaging the migration pathways for O2, CO, NO, and Xe inside myoglobin. *Biophys. J.* 91:1844–1857.

16. Gautier, R., A. Bacle, …, B. Antonny. 2018. PackMem: a versatile tool to compute and visualize interfacial packing defects in lipid bilayers. *Biophys. J.* 115:436–444.

17. Adams, P. D., P. V. Afonine, …, P. H. Zwart. 2010. PHENIX: a comprehensive Python-based system for macromolecular structure solution. *Acta Crystallogr. D Biol. Crystallogr.* 66:213–221.

18. Winn, M. D., C. C. Ballard, …, K. S. Wilson. 2011. Overview of the CCP4 suite and current developments. *Acta Crystallogr. D Biol. Crystallogr.* 67:235–242.

19. Villa, E., and K. Lasker. 2014. Finding the right fit: chiseling structures out of cryo-electron microscopy maps. *Curr. Opin. Struct. Biol.* 25:118–125.

20. Kim, D. N., and K. Y. Sanbonmatsu. 2017. Tools for the cryo-EM gold rush: going from the cryo-EM map to the atomistic model. *Biosci. Rep.* 37:BSR20170072.

21. Greengard, L., and J. Lee. 2004. Accelerating the nonuniform fast fourier transform. *SIAM Rev.* 46:443–454.

22. Hirai, T., K. Mitsuoka, …, Y. Fujiyoshi. 2007. Simulation of charge effects on density maps obtained by high-resolution electron crystallography. *J. Electron Microsc.* 56:131–140.

23. Briones, R., C. Aponte-Santamaría, and B. L. de Groot. 2017. Localization and ordering of lipids around aquaporin-0: protein and lipid mobility effects. *Front. Physiol.* 8:124.

24. Aponte-Santamaría, C., G. Fischer, …, B. L. de Groot. 2017. Temperature dependence of protein-water interactions in a gated yeast aquaporin. *Sci. Rep.* 7:4016.

25. Pluhackova, K., S. Gahbauer, …, R. A. Böckmann. 2016. Dynamic cholesterol-conditioned dimerization of the G protein coupled chemokine receptor type 4. *PLoS Comput. Biol.* 12:e1005169.

26. Song, C., C. Weichbrodt, …, K. Zeth. 2013. Crystal structure and functional mechanism of a human antimicrobial membrane channel. *Proc. Natl. Acad. Sci. USA.* 110:4586–4591.

27. Gonen, T., Y. Cheng, …, T. Walz. 2005. Lipid-protein interactions in double-layered two-dimensional AQP0 crystals. *Nature.* 438:633–638.

Briones et al.

28. Costello, M. J., T. J. McIntosh, and J. D. Robertson. 1989. Distribution of gap junctions and square array junctions in the mammalian lens. *Invest. Ophthalmol. Vis. Sci.* 30:975–989.

29. Hite, R. K., Z. Li, and T. Walz. 2010. Principles of membrane protein interactions with annular lipids deduced from aquaporin-0 2D crystals. *EMBO J.* 29:1652–1658.

30. Hite, R. K., P. L. Chiu, …, T. Walz. 2015. Effect of lipid head groups on double-layered two-dimensional crystals formed by aquaporin-0. *PLoS One.* 10:e0117371.

31. Aponte-Santamaría, C., R. Briones, …, B. L. de Groot. 2012. Molecular driving forces defining lipid positions around aquaporin-0. *Proc. Natl. Acad. Sci. USA.* 109:9887–9892.

32. Stansfeld, P. J., E. E. Jefferys, and M. S. Sansom. 2013. Multiscale simulations reveal conserved patterns of lipid interactions with aquaporins. *Structure.* 21:810–819.

33. Fischer, G., U. Kosinska-Eriksson, …, K. Lindkvist-Petersson. 2009. Crystal structure of a yeast aquaporin at 1.15 angstrom reveals a novel gating mechanism. *PLoS Biol.* 7:e1000130.

34. Nguyen, D. H., and D. Taub. 2002. CXCR4 function requires membrane cholesterol: implications for HIV infection. *J. Immunol.* 168:4121–4126.

35. Schittek, B., R. Hipfel, …, C. Garbe. 2001. Dermcidin: a novel human antibiotic peptide secreted by sweat glands. *Nat. Immunol.* 2:1133–1137.

36. Smart, O. S., J. M. Goodfellow, and B. A. Wallace. 1993. The pore dimensions of gramicidin A. *Biophys. J.* 65:2455–2460.

37. Sehnal, D., R. Svobodová Vařeková, …, J. Koča. 2013. MOLE 2.0: advanced approach for analysis of biomacromolecular channels. *J. Cheminform.* 5:39.

38. Brezovsky, J., B. Kozlikova, and J. Damborsky. 2018. Computational analysis of protein tunnels and channels. *Methods Mol. Biol.* 1685:25–42.

39. Gapsys, V., and B. L. de Groot. 2013. Optimal superpositioning of flexible molecule ensembles. *Biophys. J.* 104:196–207.